Dynamic Tensile Response of Additively Manufactured Ti6Al4V With Embedded Spherical Pores

Refael Fadida[1]
Rafael,
POB 2250,
Haifa 3102102, Israel
e-mail: fadidarafi@gmail.com

Amnon Shirizly
Rafael,
POB 2250,
Haifa 3102102, Israel

Daniel Rittel
Faculty of Mechanical Engineering,
Technion,
Haifa 3200003, Israel

The dynamic tensile response of additively manufactured (AM) dense and porous Ti6Al4V specimens was investigated under quasi-static and dynamic tension. The porous specimens contained single embedded spherical pores of different diameters. Such artificial spherical pores can mimic the behavior of realistic flaws in the material. It was found that beyond a certain pore diameter (Ø600 μm), the failure is determined according to the pore location, characterized by an abrupt failure and a significant decrease of ductility, while below that diameter, necking and fracture do not occur at the pore. The dynamic tensile mechanical behavior of the additively manufactured dense material was found to be similar to that of the conventional equivalent material, but the ductility to failure of the latter is observed to be higher. [DOI: 10.1115/1.4039048]

Keywords: additive manufacturing, titanium alloys, porous material, dynamic behavior, Ti6Al4V

1 Introduction

Additive manufacturing (AM) of metals is increasingly considered as a viable alternative to conventional manufacturing processes in a growing number of applications. The term "3D printing" is usually used as a synonym for additive manufacturing, as the latter better describes the character of the fabrication technique. Unlike conventional machining processes involving material removal, the printed part is built layer-by-layer using high power energy source, such as laser or electron beam. The technology allows the fabrication of fully dense material with mechanical properties comparable to the same material made by conventional fabrication [1–3]. One of the many advantages of AM is the ability to fabricate any geometry, including those previously impossible or too costly to be manufactured by conventional technologies. Porous materials, for example, can be fabricated in a controlled manner to achieve any pore geometry and connectedness, while with other processing methods, this capability is simply impossible. Today, additive manufacturing technology has largely reached industrialization stage. Let us note here the medical and aerospace industries, among others, that have already moved to commercial scale production. Several testing standards have been published [4–6], which allow comparing between components coming from different sources of additive manufacturing technology. In practice, scientists and engineers crave for any information that can expand the knowledge on the properties and behavior of additively manufactured materials, while their standardization is still maturing. While most of the available body of knowledge concerns quasi-static loading, the dynamic response of materials at high strain rate is quite important for a variety of applications [7–9]. While the dynamic behavior of conventionally processed titanium and other metals is well known in the literature [10–12], the behavior of additively manufactured metals at high strain rates is still relatively unexplored. Recently, Jones et al. [13] investigated the spall strength of additive manufactured Ti6Al4V processed by selective laser melting (SLM^{TM}) technique. They found that when the tensile load was applied normal to the interfaces between the AM build layers, the spall strength was reduced to 60% of that of the wrought material; however, when loaded parallel to the building layers, the spall strength was found to remain at 95% of the wrought material. Matthes et al. [14] studied the behavior of Ti6Al4V, processed by electron beam additive manufacturing (EBAM^{TM}) technology, subjected to shock loading. Fadida et al. [3] reported that the dynamic behavior of the additively manufactured Ti6Al4V, which were fabricated using the direct metal laser sintering (DMLS^{TM}), possesses a higher dynamic compressive strength than that of the conventionally processed material. Ackelid and Svensson [15] found that the mechanical and chemical properties of electron beam melting (EBM^{TM}) processed Ti6Al4V are comparable to those of wrought Ti6Al4V. Gray et al. [16] compared the spall strength of 316 L SS fabricated by laser engineered net shaping (LENS^{TM}) to that of nominal annealed wrought 316 L SS plate. It was found that the spall strength of AM-produced 316 L was very similar to that of annealed wrought 316 L. Lovinger et al. [17] examined the shear band evolution in a thick-walled cylinder Ti6Al4V fabricated by laser metal deposition (LMD^{TM}). Recent studies have shown that additive manufacturing can be a very helpful tool in the investigation of porous materials [18–24]. In some studies, porosity was achieved by variation of the process parameters (such as laser power and scanning speed), while in others, the pore shape and distribution was fabricated according to a specific computer-aided design (CAD) model. Common to all is the investigation of highly porous structures with a closed or opened content. Since the seminal model of Gurson [25], which analyzes plastic flow in a porous medium, numerous studies have investigated the effects of voids on ductile fracture as described in great detail in the review of Benzerga and Leblond [26]. Since three-dimensional (3D) voids are hard, not to say impossible, to create with the current technologies, most researchers have investigated specimens, which contain two-dimensional voids (e.g., holes) [27–30]. To date, experimental studies, which are investigating the behavior of a single 3D void (or the interaction of an array) using AM technique, are still missing. Generally, it seems that the lack of appropriate technology to fabricate 3D voids and the increase of computing power have mostly favored analytical and numerical modeling studies so far. According to Benzerga and Leblond [26], recent 3D models are too complex to implement by engineers, along with the lack of selective experiments for comparison

[1]Corresponding author.

Contributed by the Applied Mechanics Division of ASME for publication in the Journal of Applied Mechanics. Manuscript received November 7, 2017; final manuscript received January 14, 2018; published online February 2, 2018. Editor: Yonggang Huang.

purposes with analytical predictions. Many researches have experimentally addressed static and dynamic behavior of conventional porous materials [31–34]. Unfortunately, publications concerning porous materials fabricated by additive manufacturing, and subjected to dynamic loading, are still quite scarce. Biswas et al. [18] investigated the deformation of dense and porous laser engineered net shaping (LENS) Ti6Al4V under dynamic compression loadings. Fadida et al. [3] explored the dynamic behavior of additively manufactured dense and porous Ti6Al4V. The porous specimens contained spherical voids with full control on the geometry and location of pores and relatively high dimensional accuracy. The authors suggested that the pores' orientation with respect to the load direction should also be considered as an important parameter to be included in analytical failure models of porous materials. However, there is no study reporting the behavior of a single pore containing structure under dynamic loading. Therefore, the present study presents dynamic tension results and modeling of specimens containing a single spherical void, whose diameter is systematically varied.

This paper is organized as follows: Section 2 describes the experimental framework used to evaluate the mechanical response of the additively manufactured material. Section 3 provides the experimental results. Section 4 deals with numerical simulations. Section 5 then discusses in the experimental and numerical results. Finally, Sec. 6 presents summary and conclusions.

2 Experimental Setup

2.1 Dynamic Tension Tests. The principles for testing materials at high strain rates in tension are similar to those of the compression test, using as the split Hopkinson pressure bar, first introduced by Kolsky in 1949 [35] and further developed by Harding et al. [36]. While in the compression test, the cylindrical specimen is sandwiched between two long bars, in the tension apparatus, the specimen is threaded to be inserted into the two bars. The tensile pulse is generated by shooting a hollow striker tube against a flange ending the incident bar, all made of hardened C300 maraging steel. The stress waves are measured by means of strain gauges cemented on midlength on the incident and transmitted bars. The three strain pulses that are measured are incident, reflected, and transmitted. The forces on both sides of the specimen are calculated based on the measured strains and verified for equilibrium. The resulting stress–strain curve is deemed to be valid if dynamic force equilibrium is achieved. The basic equations used for data reduction of the split Hopkinson tensile bar tests can be found in Appendix.

2.2 Specimen Design

2.2.1 Fully Dense Specimen. The fully dense additively manufactured material Ti6Al4V was fabricated using the DMLS technology, which uses a high power laser source to turn a metal powder into a solid part. The CAD model of the desired part is virtually sliced into numerous layers using dedicated software. The part is processed in an argon-filled chamber. A uniform thin layer of powder, usually tens of microns thick, is placed down on a solid substrate made of the same material. The laser source melts the pattern that represents the solid in each layer. When the first layer is finished, the part lowers down, the next powder layer is deposited, the next layer melts, and so on until completion of the part. An 18 mm thick, cold rolled annealed plate of premium-quality Ti6Al4V was chosen to provide a reference for the additively manufactured material. The gauge diameter and the gauge length were set to $d_0 = Ø4\,\text{mm}$ and $l_0 = 16\,\text{mm}$, respectively, based on Rotbaum and Rittel [37]. The specimens were designed to be almost identical in their geometrical dimensions. The typical tolerance for specimen's gauge diameter and gauge length was of the order of $\pm 0.05\,\text{mm}$. Figure 1 shows a generic sketch of the specimen for dynamic tensile test and its appearance after machining. The surface roughness of the additively manufactured material

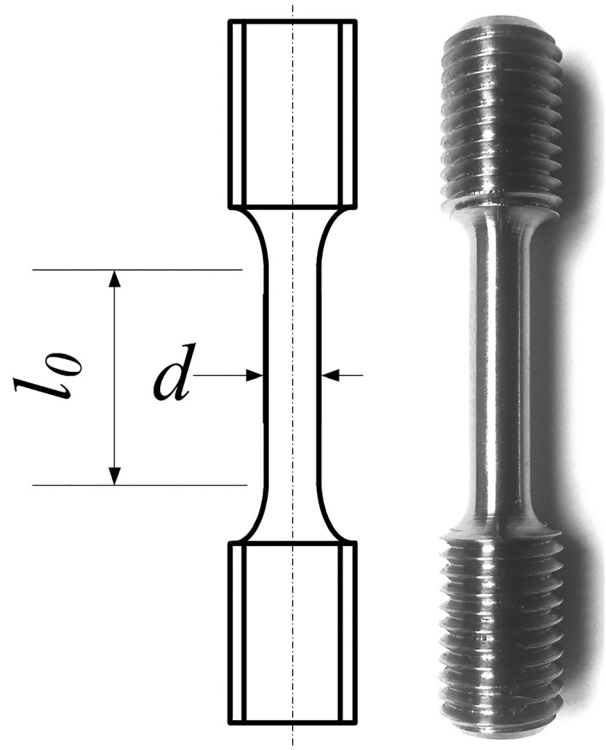

Fig. 1 A sketch and typical printed tensile specimen after machining

is known to be coarse; therefore, the specimen was lightly machined to remove any surface flaw that might affect the results.

2.2.2 Single Pore Specimen. The geometrical resolution of structural features (e.g., walls, holes, pins, arcs, struts etc.), manufactured by laser-based additive manufacturing technology is mainly determined by the laser spot size, layer thickness, and powder characteristics [38]. Design rules for additive manufacturing can be easily found in the literature [39] but guidelines for the fabrication of internal closed 3D voids are still absent. Figure 2 shows a reference specimen, which was specially designed to assess the size and shape of enclosed spherical pores, to test the system's performance. The smallest pore size, with respect to the specimen dimensions, is desired in order to mimic realistic flaws in the material however; X-ray resolution need to be taken into account for practical reasons, making sure that the flaw can be imaged prior to testing. It can be observed that down to 300 μm diameter, pores can be visually differentiated from the fully dense material but, the spherical shape of the smallest pores becomes much less accurate geometrically. The content of inner closed volumes stays in powdery state at the end of the manufacturing process. This residual powder was assumed to have negligible effect on the mechanical tests results [3].

Figure 3 shows X-ray images of a set of specimens that contain a single pore located at the geometric center of the specimen. The pores were fabricated according to the CAD model in the following dimensions Ø300, Ø400, Ø500, Ø600, Ø700, and Ø1000 μm, respectively. As mentioned, the specimen gauge diameter was set to Ø4 mm, which is approximately one order of magnitude compared to the smallest pore size. Necking is known to be a local phenomenon; therefore, the volume fraction of the pore was calculated with respect to a theoretical sphere, whose diameter equals the specimen gauge diameter, as illustrated on Fig. 4. Table 1 summarizes the volume fraction of the pore, which was calculated according to

$$f = \frac{V_{\text{void}}}{V_{\text{material}}} \tag{2.1}$$

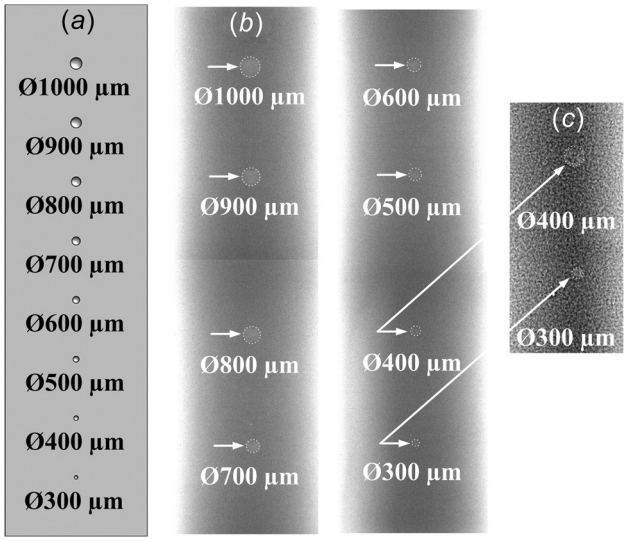

Fig. 2 A reference specimen for evaluating the optimal pore shape and diameter. (*a*) The cross section of the CAD model, (*b*) the X-ray imaging, and (*c*) the Ø300 and Ø400 μm pore at higher magnification. Note that Ø300 μm is the lower limit of feasible pores in the current setup.

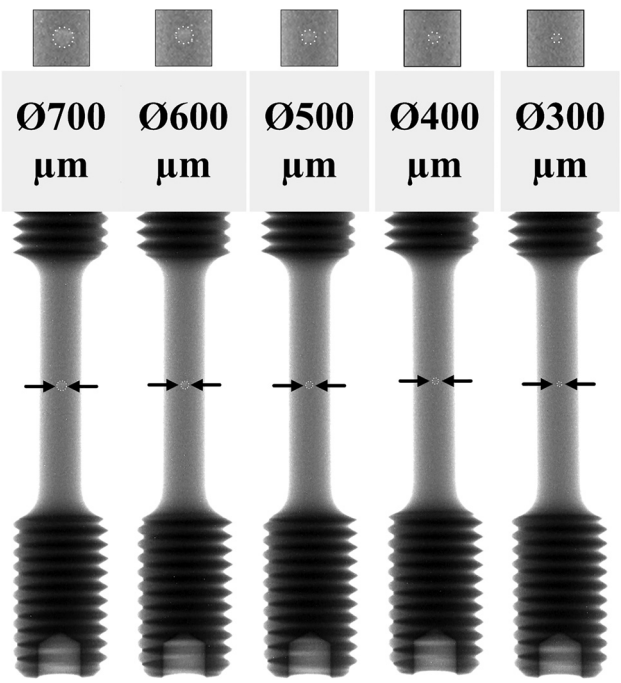

Fig. 3 A set of additively manufactured specimens, which contain an enclosed pore (outlined) with different diameters. The pore is located at the geometrical center of the gauge section. Note the shape of the pore, which is relatively spherical.

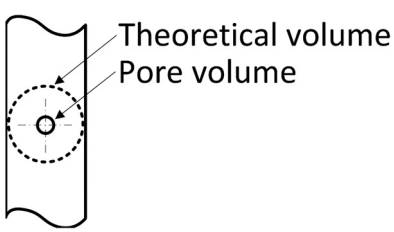

Fig. 4 The pore is concentric to a theoretical sphere, which determines the volume fraction of the pore

Table 1 The calculated volume fraction of the single pore specimens

Pore size (μm)	Pore volume fraction (%)
Ø300	0.04
Ø400	0.10
Ø500	0.20
Ø600	0.34
Ø700	0.54
Ø1000	1.56

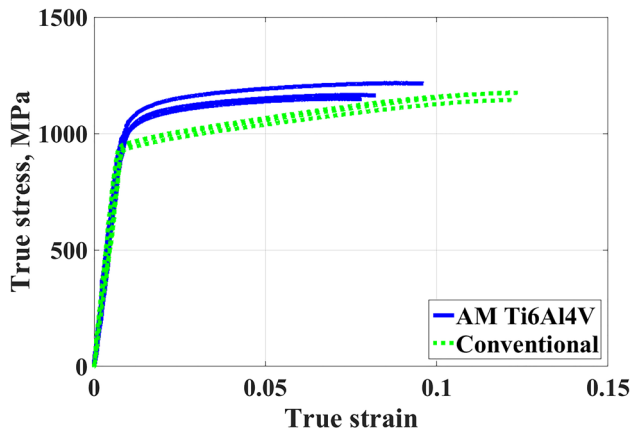

Fig. 5 Additively manufactured Ti6Al4V compared to conventional material in quasi-static tension at nominal strain rate of 2×10^{-4} s^{-1}. The graph represents the uniform elongation part, prior to necking.

where V_{void} is the volume of the pore and V_{material} is the volume of the theoretical sphere.

3 Experimental Results

3.1 Quasistatic Tension of Fully Dense Ti6Al4V. Quasi-static tensile testing was performed to measure the mechanical properties of the additively manufactured material and compare it to the conventional material. A set of three specimens of each material type (i.e., cold-rolled and annealed versus AM) were tested at a nominal strain rate of 2×10^{-4} s^{-1}. Figure 5 shows the comparison between AM Ti6Al4V and conventional material, noting that the plots represent the uniform elongation stage until the onset of necking. As can be seen, the tensile yield strength of the AM material is higher than that of the conventionally processed material. The tensile yield strength of the AM material and the conventional material was 1020 ± 31 MPa and 947 ± 8 MPa, respectively. The difference in tensile yield strength stress exceeds 7% in favor of the AM material. The yield strength of the reference material is similar that reported in the literature [40]. The calculated Young's modulus of the AM material was 117 GPa, which is similar to that of the conventional material, 114 GPa. The AM material exhibits a limited strain hardening capacity with respect to the conventional one. Both materials exhibit the typical cup-and-cone shaped failure surface.

3.2 Dynamic Tension of Fully Dense Ti6Al4V. A set of four specimens of each material type were tested at nominal strain rate of 1×10^3 s^{-1}. The specimen gauge length and gauge diameter were same as for the quasi-static tests. Figure 6 shows the comparison between the AM material and the conventional material at comparable strain rates. The AM material exhibits a slightly higher strength than the conventionally processed material. The

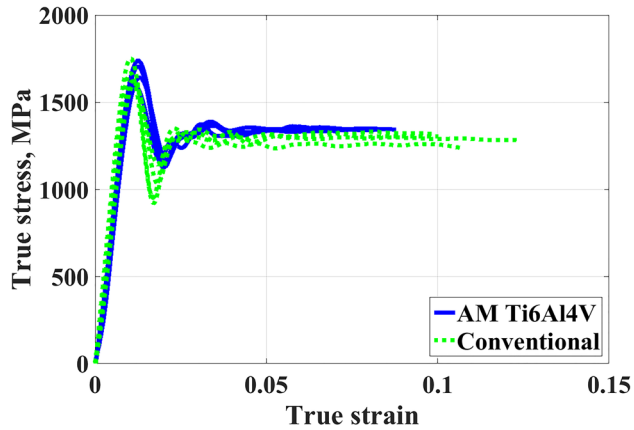

Fig. 6 Additively manufactured Ti6Al4V compared to conventional material in dynamic tension at nominal strain rate of 1×10^3 s^{-1}. The graph represents the uniform elongation part, prior to necking.

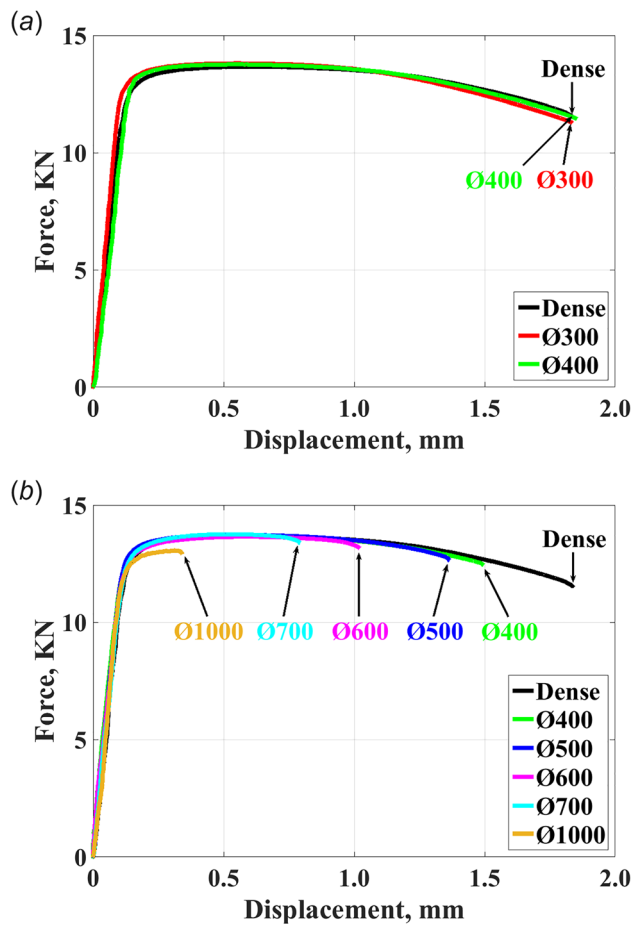

Fig. 7 A single pore specimens in quasi-static tension with different pore diameter at nominal strain rate of 2×10^{-4} s^{-1}. (*a*) All the Ø300 μm specimens and one Ø400 μm specimen did not fail at the pore (similar to the dense specimens behavior). (*b*) One Ø400 μm specimen and all the Ø500, Ø600, Ø700, and Ø1000 μm specimens failed at the pore.

measured flow stress for the AM material and the conventional material at $\varepsilon = 0.05$ is about 1340 ± 5 MPa and 1284 ± 45 MPa, respectively. The difference in flow stress exceeds 4% in favor of the AM material. All in all, both materials perform almost identically in dynamic tension.

Table 2 A summary of the quasi-static tensile test results

Specimen type	Failure location
Fully dense	Close to midgauge length
Single pore Ø300 μm	Close to midgauge length
Single pore Ø400 μm	Only one failed at the pore
Single pore Ø500 μm	All failed at the pore
Single pore Ø600 μm	All failed at the pore
Single pore Ø700 μm	All failed at the pore
Single pore Ø1000 μm	All failed at the pore

3.3 Quasi-Static Tension of Single Pore Specimens. Quasi-static tests were performed on the single pore specimens at a nominal strain rate of 2×10^{-4} s^{-1}. Figure 7 shows the load displacement results. Each curve represents the typical behavior of two specimens, which responded almost identically. The Ø300 μm specimens did not fail at the pore, while only one Ø400 μm specimen failed at the pore, whose curve is represented in Fig. 7(*b*). The Ø500, Ø600, Ø700, and Ø1000 μm specimens all failed at the pore. A clear decline in displacement to failure can be seen when the pore size increases, while changes in load can barely be observed. A slight reduction in load can be seen only for the Ø1000 μm curve. Table 2 lists the results of the quasi-static tests carried out on fully dense and single pore specimen.

3.4 Dynamic Tension of Single Pore Specimens. The specimens containing a single pore of different diameters were subjected to dynamic tension loading at a nominal strain rate of 1×10^3 s^{-1}. A set of four specimens of each type were tested. Figure 8 shows the load–displacement behavior resulting from a single spherical pore located at the geometric center of the specimen. For each set, the differences in flow stress were quite minor while the differences in elongation to failure are clearer. The specimens containing the Ø600, Ø700, and Ø1000 μm pore all *failed at the pore*. By contrast, only one specimen containing Ø500 μm pore failed at the pore, while the others did not fail at the pore. For the specimens that did not fail at the pore, fracture occurred close to the impacted side. Exceptionally, one Ø500 μm specimen failed at the opposite side (i.e., at the transmitted side). Table 3 lists the results of the dynamic tests carried out on fully dense and single pore specimen. Figure 9 shows an X-ray image of two Ø500 μm specimens that did not fail at the pore compared to an undeformed specimen. Specimens that failed at the pore exhibit a unique cone shape, which starts from the pore's crater and expands to the outer surface of the specimen, as shown in Figs. 10 and 11. Figure 12 shows an image of the fractured specimen in dynamic test taken from a high speed camera recording. It is clear that the content of the pore is in the powdery state and not solid. Figure 13 summarizes the results shown on Fig. 8 with reference to the fully dense specimen. A clear decline in displacement to failure, compared to the dense material, can be seen at the Ø600, Ø700, and Ø1000 μm specimens. This trend changes from the Ø500 μm pore and below. Although there is a great similarity between the Ø300, Ø400, Ø500 μm and the dense specimen prior to necking, a variance in displacement to failure is quite notable. Recall that these specimens did not fail at the pore; therefore, the failure is determined according to the dynamics of the stress waves and not by the pore itself, similar to the results reported by Rittel et al. [41] in which notched specimens failed away from the notch location. Figure 14 presents the results of Fig. 13 plotted this time as a function of pore volume fraction. From Fig. 14, it appears that from Ø600 μm, the decline in displacement is dramatic compared to the dense results (indicated as 0% pore volume fraction).

4 Numerical Simulations

Numerical simulations were conducted using commercial finite element software (ABAQUS explicit FE software [42]). The model

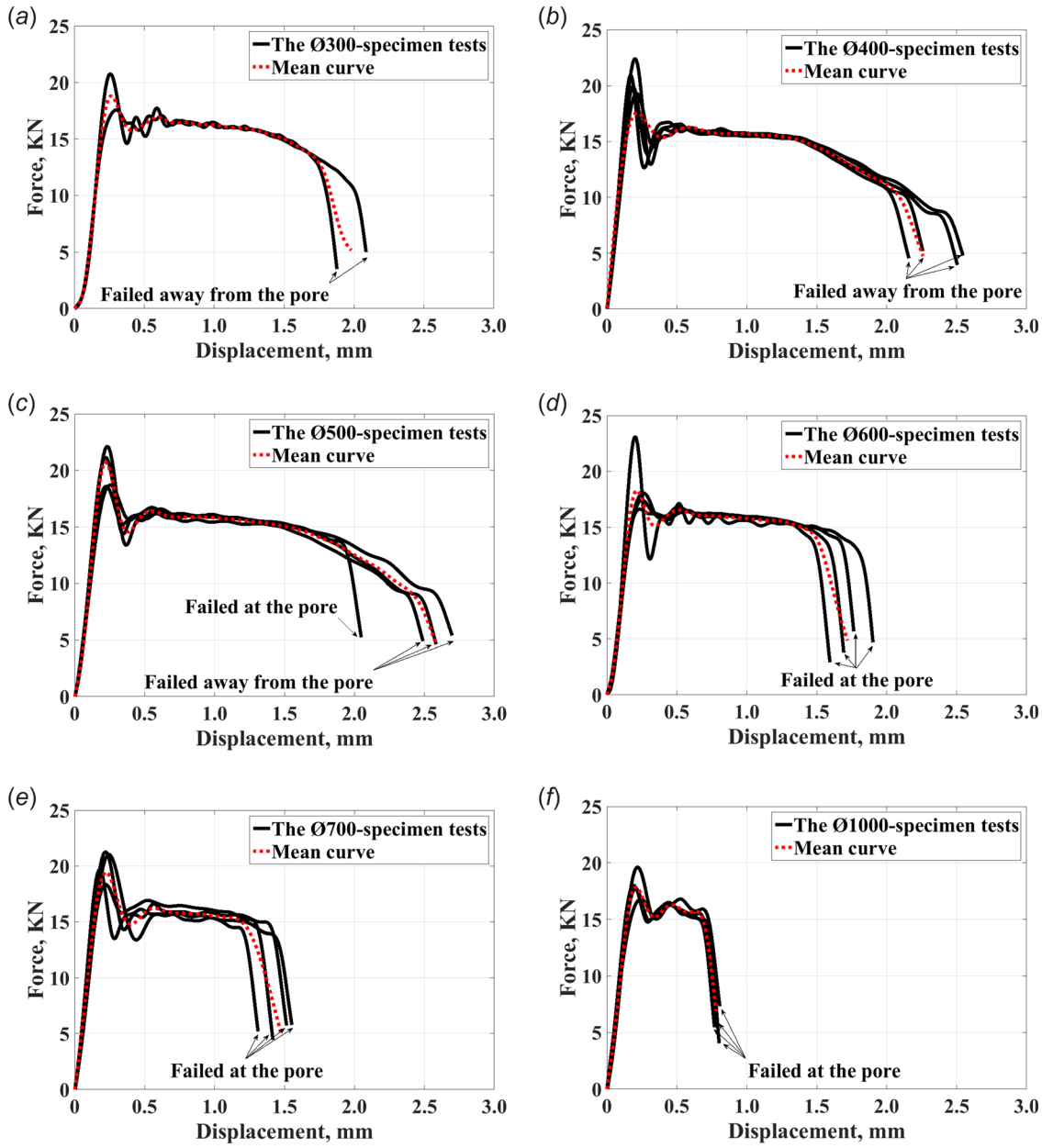

Fig. 8 Load displacement curves of all single pore specimen type i.e., Ø300, Ø400, Ø500, Ø600, Ø700, and Ø1000 μm at nominal strain rate of 1×10^3 s^{-1}. The red line in each figure represents the mean curve of all tests. Above Ø500 all specimens failed at the pore without exceptions. The displacement to failure was determined by drawing a line, which is parallel to the linear elastic response, at the point before the force rapidly drops.

Table 3 A summary of the dynamic tensile tests results

Specimen type	Failure location
Fully dense	Close to midgauge length
Single pore Ø300 μm	Close to midgauge length
Single pore Ø400 μm	Close to midgauge length
Single pore Ø500 μm	Only one failed at the pore
Single pore Ø600 μm	All failed at the pore
Single pore Ø700 μm	All failed at the pore
Single pore Ø1000 μm	All failed at the pore

of the dynamic tensile test apparatus was axisymmetric and included the incident bar, transmitted bar, and the fully bounded specimen. The velocity boundary condition was applied at the free end of the incident bar to mimic the striker's impact. The model was meshed with a four-node bilinear axisymmetric quadrilateral element, with a typical size of 1000 μm along the incident and transmitted bars and 30 μm along the specimen gauge. A typical meshing of a specimen with a single pore is shown in Fig. 15. The AM material behavior up to necking was described according to the J2 plasticity with isotropic hardening, while the behavior after necking was obtained using the software implementation for ductile damage model [42]. The material's plastic behavior was curve fitted according to the dynamic tensile tests, previously described (Fig. 6), using the following power law hardening material model:

$$\sigma = \sigma_0 + K\varepsilon_p^n \tag{4.1}$$

where σ_0 is the approximate value of the dynamic yield stress, ε_p is the plastic strain, and K and n are dimensionless parameters. It was assumed that the damage model is not strain rate dependent,

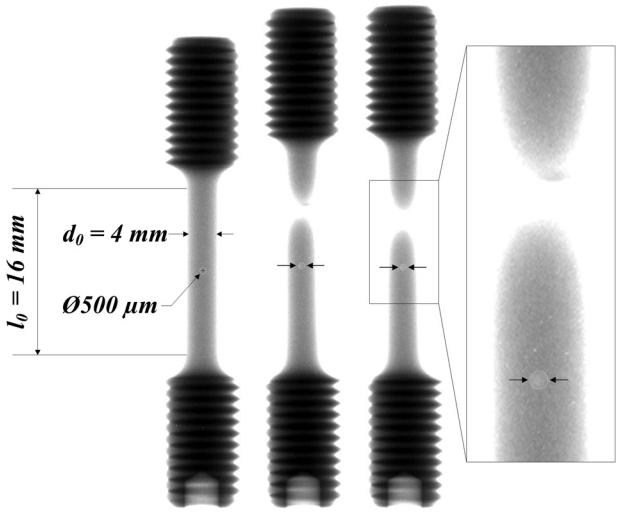

Fig. 9 X-ray image of an additively manufactured specimen contains Ø500 μm pore. Two deformed specimens on the right, compared to an undeformed specimen on the left. Note that the fracture occurred not at the pore.

but based on a critical value of the equivalent fracture strain at damage initiation, $\bar{\varepsilon}^{pl}$. The model parameters are summarized in Table 4. At first, iterative process was performed until the numerical results of the fully dense material were found to fit well with the experimental data in terms of force–displacement behavior, and then the same parameters were applied to the single-pore specimen models.

The simulation results reproduce the experimental observations, as shown in Fig. 16. The force–displacement behavior up to necking is similar for most pore sizes, except for the Ø1000 μm. The displacement where the neck begins is similar for most of the specimens and its value is similar to that obtained in the experiments. The simulations show that necking occurs at the same location of the pore starting from 500 μm pore. In other words, for pore diameter smaller than 500 μm, the calculated failure occurs away from the pore (i.e., at the impacted side), and above that diameter, all specimens failed at the pore. This result is similar to the experiments, which indicate that the occurrence of necking at the pore is not random, but is rather related to the geometric dimensions of the pore. Additionally, the simulation reproduced the observed cup and cone fracture, showing that fracture initiates at the pore and expends to the outer surface of the specimen creating a slant path, as can be seen in Fig. 17. The simulation clearly shows that the larger the pore, the smaller the elongation to failure. Exceptionally, the experimental results of Ø300, Ø400, and Ø500 μm (which did not fail at the pore), compared to the fully dense material, do not show a clear trend, and that is probably due to small differences in boundary condition. As mentioned above, both the simulations and experiments show that from certain pore diameter (or in general, from certain pore volume fraction), the pore determines the locus of fracture rather than the interaction of stress waves. That case is characterized by a significant reduction of ductility up to failure and a unique cup and cone fracture

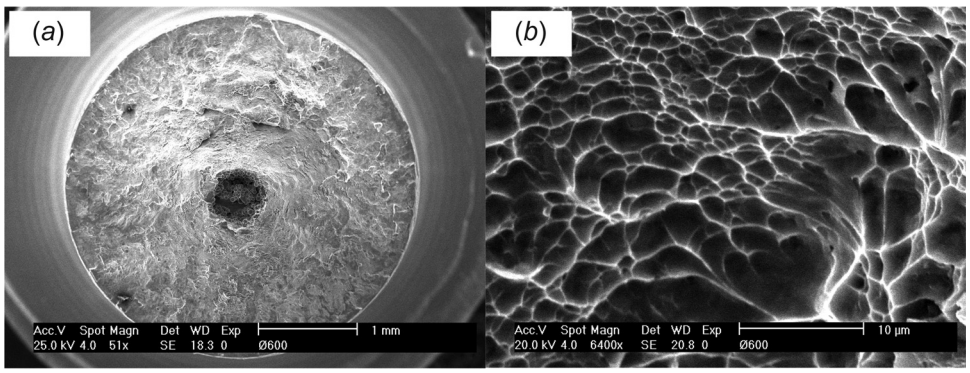

Fig. 10 A SEM image of a specimen contains Ø600 μm pore after failure. (*a*) The trace of the pore in the top of the cone can be clearly seen. (*b*) A typical view of the cone surface characterized by dimples indicates ductile fracture.

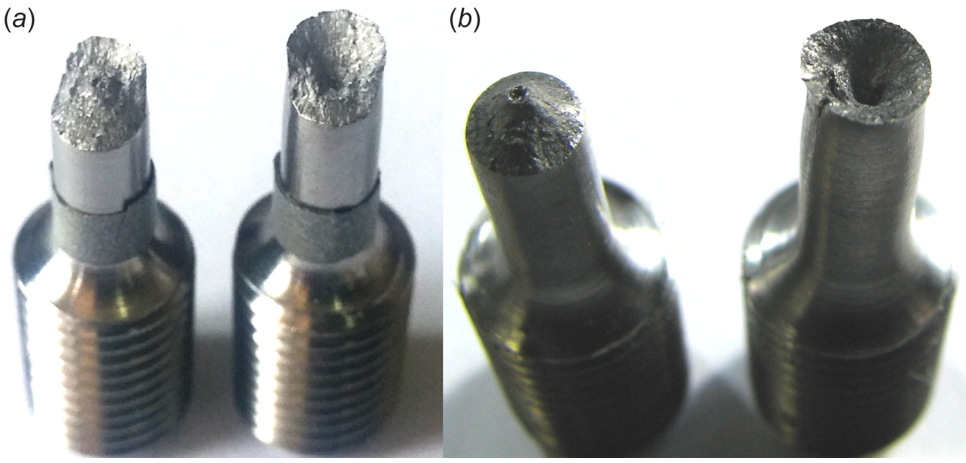

Fig. 11 A typical fractography of a specimen contain Ø600 μm pore after tensile test. (*a*) Quasi-static loading. (*b*) Dynamic loading.

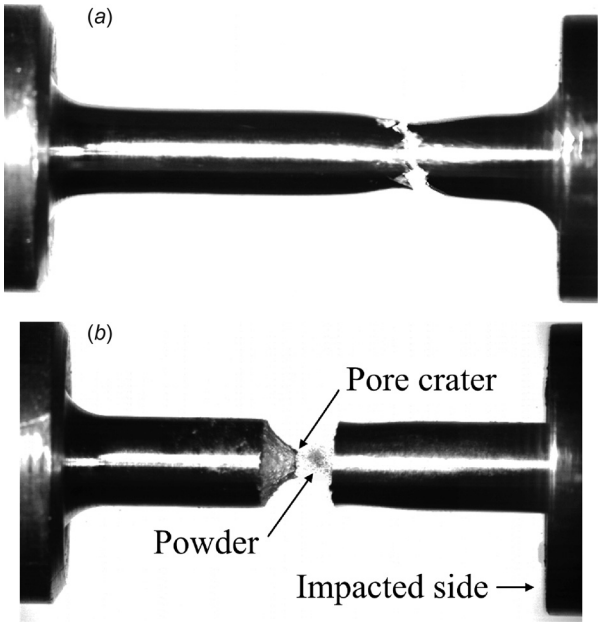

Fig. 12 High speed camera image of specimens at dynamic tensile test. (*a*) Fully dense AM Ti6Al4V. The fracture occurred at the impacted side. (*b*) A Ø1000 μm pore at the moment of fracture. Note the residual powder that was released out, which proves that the pore content is not solid (i.e., in powdery state).

surface morphology. Figure 18 shows a comparison of force and displacement of experiment and numerical simulation for the fully dense Ø600 and Ø700 μm pore. It can be noted that until the onset of final fracture, the simulations and experiments agree quite well. Proper replication of the final fracture stage will necessitate additional future work.

5 Discussion

The yield strength of the AM Ti6Al4V is found to be higher than that of its conventional equivalent, while the dynamic behavior of both conditions is similar, with advantage for the AM material. However, in both regimes, the conventional material is found to be more ductile than the AM material. It should be pointed out that the ductility of the AM material can be improved at the expense of strength by applying HIP process [43]. These results emphasize the quality of the AM Ti6Al4V, which is fabricated by the DMLS technology. The originality of this study lies on the investigation of 3D-voids, which were deliberately embedded in tensile specimens. For this purpose, this technology was found to be suitable, as it was in compression experiments [3]. In the dynamic tests, it was shown that necking occurs at the pore location starting from Ø600 μm and above, while below that diameter (i.e., Ø300–Ø500 μm), necking and fracture develop away from it, mostly on the impacted side. These results are similar to those reported by Rittel et al. [41] who showed that stress–wave interactions determined the neck location away from a geometrical disorder flaw (notch), which was deliberately located at the gauge midlength. Moreover, it was shown that this behavior is sensitive to the boundary conditions, namely impact velocity. With that, the lack of notch sensitivity was observed for notches that were not relatively deeper than 0.1 times the diameter. It is interesting to note that in the present experiments, the "transition" pore diameter is of the order of 0.15 times the specimen diameter, which just suggests that despite the different context, the same phenomenon reproduces itself. Artificial imperfections, such as (machined) notch, mimic only surface defects. After machining processes, defects (such as inclusions) are still present inside the material, which under external loads grow, coalesce, and eventually lead to

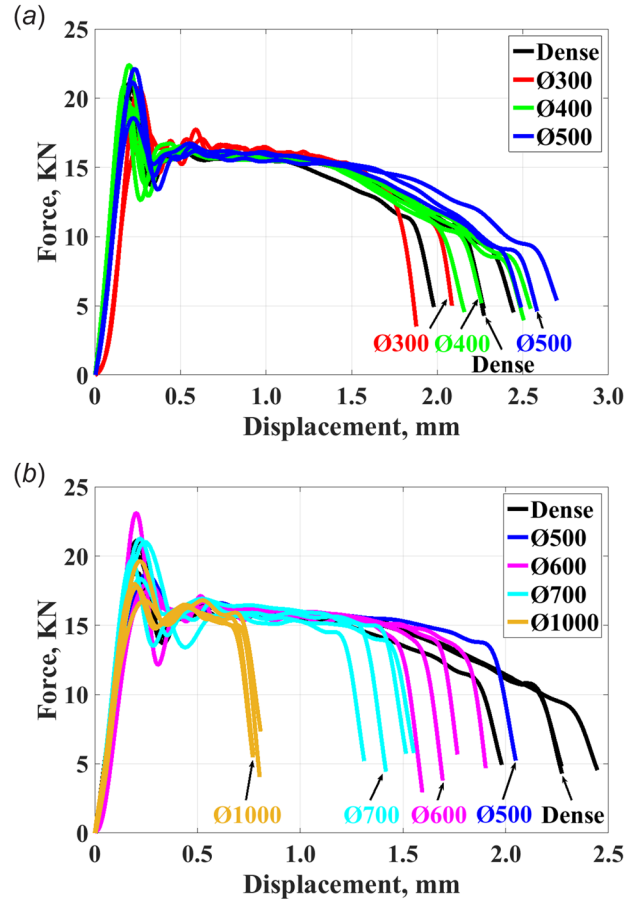

Fig. 13 Single pore specimens in tension with different pore diameter at nominal strain rate of 1×10^3 s^{-1}. (*a*) All the Ø300, Ø400, and most Ø500 μm specimens failed away from the pore. Note that all the curves tend to cluster around the dense specimen curves. (*b*) Only one Ø500 μm specimen and all the Ø600, Ø700, and Ø1000 μm specimens failed at the pore. (The arrows indicate a typical curve based on the average curve represented in Fig. 8). Here, a clear decline in displacement to failure can be noticed with increasing pore diameter.

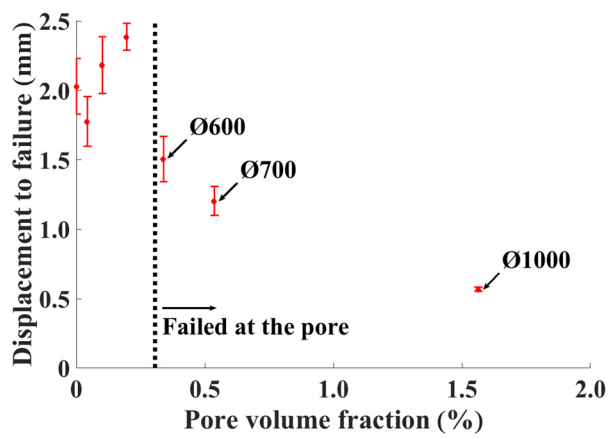

Fig. 14 Displacement to failure as a function of pore volume fraction for a single pore specimen under dynamic loading. The vertical dashed line separates between the specimens that failed at the pore and the ones who did not. The displacement to failure at zero porosity represents the dense material.

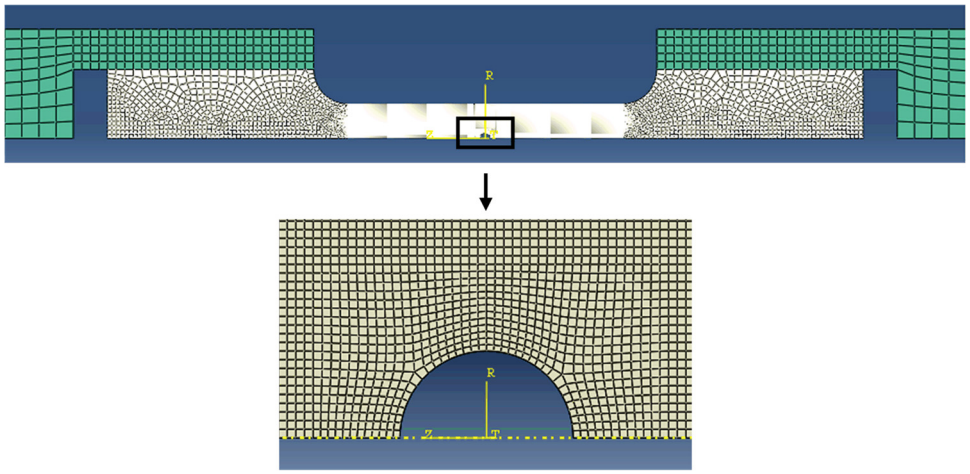

Fig. 15 The mesh of the numerical model. The specimen (additively manufactured Ti6Al4V), which contain a single pore Ø600 μm and the incident and the transmitted bars (maraging 300).

Table 4 Parameters used to describe the constitutive behavior of the AM material

σ_0	K	N	$\bar{\varepsilon}^{pl}$
1125 (MPa)	470.9	0.264	18%

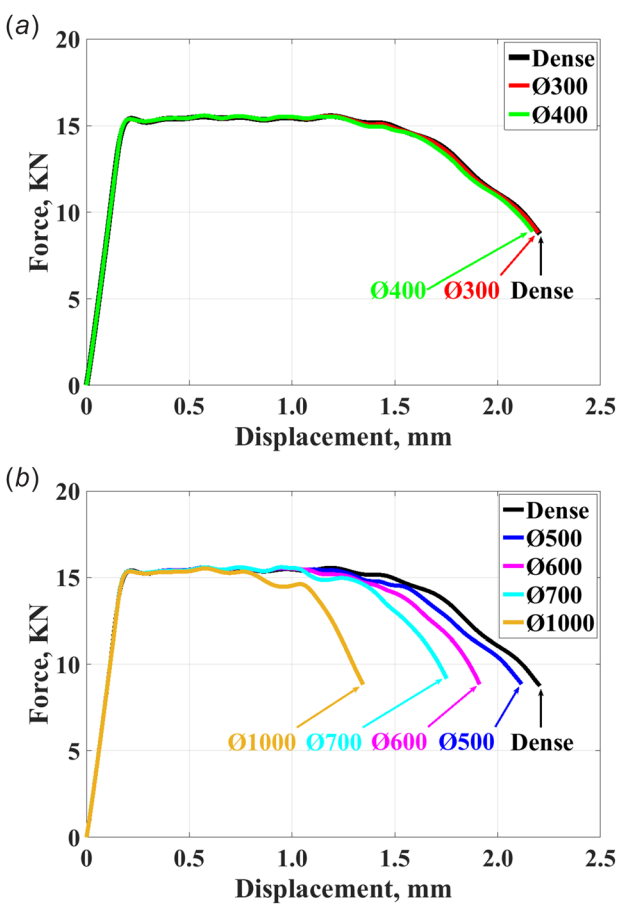

Fig. 16 The numerical simulation results for the fully dense and the single-pore specimens. (*a*) The Ø300 and Ø400 μm specimens failed away from the pore. (*b*) The Ø500, Ø600, Ø700, and Ø1000 μm specimens failed at the pore.

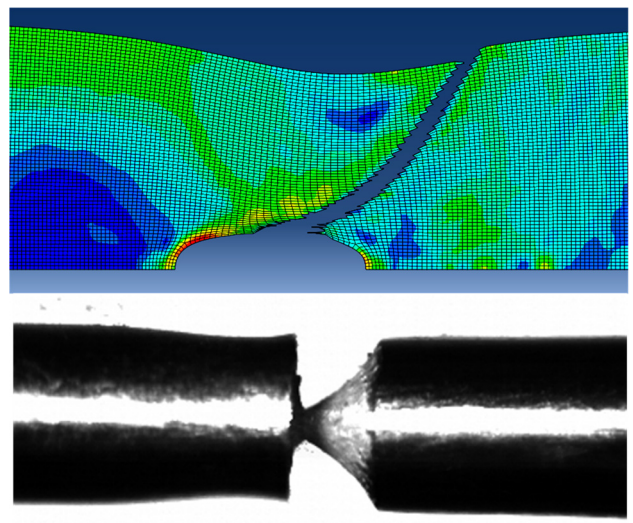

Fig. 17 At the top, a Ø600 μm pore at the moment of fracture. Note that the simulation captures the cup and cone pattern that was observed in experiments. The neck in the simulation is noticeable, although in practice it is quite limited (as can be seen at the bottom). This can explain the bias between simulation and experimental results.

fracture. Here is the place where the additive manufacturing technology shows a clear advantage. Imperfections can be fabricated in (almost) any shape and anywhere inside the specimen. The presence of a pore affects the nature of the failure, in a way that necking becomes quite limited and thus final failure become more abrupt. Simulations show the same trend and confirm that the pore has a definite influence on the dynamic behavior only from a certain pore diameter, here Ø600 μm. In the quasi-static tests, the pore becomes dominant at smaller pore sizes i.e., Ø500 μm. For both regimes, the displacement to fracture decreased significantly from Ø600 μm and above. A unique fracture feature was observed when the necking occurs at the pore. Namely, the fracture is characterized by a conical surface originating at the pore toward the outer surface of the specimen. From Fig. 14, it appears that the displacement to failure of those specimens that did not fail at the pore does not seem to exhibit a well-defined trend. Since failure occurs at locations other than the pore, one can reasonably assume that it is the combined result of the stress–wave interaction and

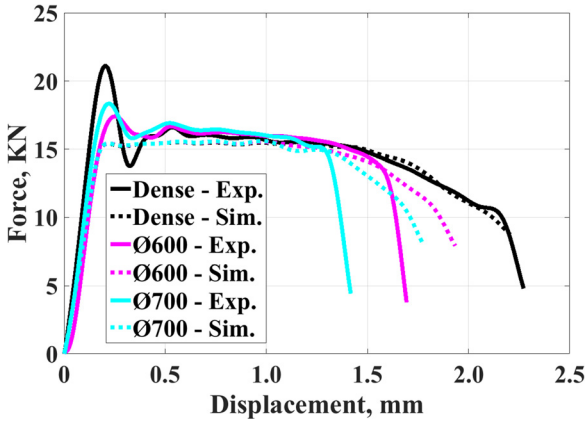

Fig. 18 The simulation corresponded well with the force–displacement response of the dense specimens, but from Ø600 μm and above some deviation is observed regarding final specimen failure

minor variations in impact velocity. By contrast, when failure occurs at the pores, a well-defined exponential decay of the displacement to failure can be noticed. This observation can be intuitively rationalized based on strength of materials considerations, with a markedly lesser sensitivity to the boundary conditions. Finally, comparing the dynamic compression results of single pore specimens reported by Fadida et al. [3] to the current results shows interesting insights. The first is that whereas all compression specimens fail through a shear mechanism involving the pore, the tensile ones "see" the pore only when its diameter exceeds 600 μm. Next, if the pore volume fraction is expressed now as the ratio between pore diameter (d) and specimen diameter (D) to unify compression and tension, one can note that the displacement to failure starts to decrease visibly from the same ratio of $d/D \approx 0.15$. Those observations point to a "critical pore size" (ratio of diameters) that acts as a game changer in tension and compression alike.

6 Conclusions

A systematic examination of spherical pores of different diameter under dynamic tensile loading shows the existence of critical pore size limit, above which the material properties are significantly reduced due to the presence of flaws.

- The tensile yield strength of AM Ti6Al4V is found to be slightly higher than that of the same extruded (conventional) material, but the ductility to failure of the conventional is observed to be higher.
- Both materials, AM Ti6Al4V and conventional, exhibit a similar behavior in the high strain rate regime.
- Spherical pores down to Ø300 can be fabricated, diagnosed, and tested with the additive manufacturing technology, to mimic the behavior of realistic flaws in material.
- For both regimes, it was found that from Ø600 μm pore diameter, the failure is determined according to the pore location, characterized by an abrupt failure and a significant decrease of ductility.
- Below a certain pore diameter (here, Ø400 μm), necking and fracture do not occur at the pore, similar to observations of dynamic tension of notched specimens.
- The present observations bear a definite similarity to previous dynamic experiments on notched tensile specimens in which the notch was avoided by necking taking place elsewhere.

Acknowledgment

The authors wish to thank Mr. Y. Rotbaum, Professor S. Osovski, Mr. R. Korabi, Mr. A. Godinger, and Dr. A. Dorogoy for their valuable technical assistance and discussions.

Appendix: The Split Hopkinson Tensile Bar Formulation

The forces in the incident and the transmitted bars are given by

$$F_{\text{in}} = A_b E_b (\varepsilon_i + \varepsilon_r) \tag{A1}$$

$$F_{\text{out}} = A_b E_b \varepsilon_t \tag{A2}$$

where A_b is the cross-sectional area of the bar; E_b is the Young's modulus of the bar; and ε_i, ε_r, and ε_t are the incident, reflected, and transmitted strains, respectively.

As mentioned, equilibrium Is fulfilled when

$$F_{\text{in}} = F_{\text{out}} \tag{A3}$$

The nominal stress in the specimen is calculated by dividing the output force by the cross-sectional area of the specimen denoted as A_s

$$\sigma_s = \frac{A_b E_b}{A_s} \varepsilon_t \tag{A4}$$

Assuming that the stress waves propagate without dispersion, the measured signals at the strain gauge can be reliably use to calculate the velocities at the specimen/bar interfaces

$$\begin{aligned} v_{\text{in}} &= c_b(\varepsilon_i - \varepsilon_r) \\ v_{\text{out}} &= c_b \varepsilon_t \end{aligned} \tag{A5}$$

where c_b is the acoustic wave speed at the bars.

The nominal strain rate in the specimen is then given by

$$\dot{\varepsilon}_s = \frac{v_{\text{in}} - v_{\text{out}}}{l_0} = \frac{c_b}{l_0}(\varepsilon_i - \varepsilon_r - \varepsilon_t) \tag{A6}$$

where l_0 is the initial length of the specimen.

When dynamic force equilibrium is fulfilled, following result holds

$$\varepsilon_i + \varepsilon_r = \varepsilon_t \tag{A7}$$

Therefore

$$\dot{\varepsilon}_s = -\frac{2c_b}{l_0} \varepsilon_r \tag{A8}$$

Consequently, the nominal strain in the specimen is given by

$$\varepsilon_s = \int \dot{\varepsilon}_s dt \tag{A9}$$

Finally, the true stress and the true strain in the specimen are calculated using the standard formulations

$$\sigma = \sigma_s(1 + \varepsilon_s) \tag{A10}$$

$$\varepsilon = \ln(1 + \varepsilon_s) \tag{A11}$$

References

[1] Frazier, W. E., 2014, "Metal Additive Manufacturing: A Review," J. Mater. Eng. Perform, **23**(6), pp. 1917–1928.
[2] Rafi, H. K., Starr, T. L., and Stucker, B. E., 2013, "A Comparison of the Tensile, Fatigue, and Fracture Behavior of Ti-6Al-4V and 15-5 PH Stainless Steel Parts Made by Selective Laser Melting," Int. J. Adv. Manuf. Technol., **69**(5–8), pp. 1299–1309.
[3] Fadida, R., Rittel, D., and Shirizly, A., 2015, "Dynamic Mechanical Behavior of Additively Manufactured Ti6Al4V With Controlled Voids," ASME J. Appl. Mech., **82**(4), p. 041004.
[4] ASTM, 2014, "Standard Specification for Additive Manufacturing Titanium-6 Aluminum-4 Vanadium With Powder Bed Fusion," ASTM International, West Conshohocken, PA, Standard No. ASTM F2924-14.

[5] SAE, 2002, "Titanium Alloy Laser Deposited Products 6Al-4V Annealed," SAE International, Warrendale, PA, SAE Standard No. AMS 4999.
[6] Aumund-Kopp, C., and Petzoldt, F., 2016, "Standards for Metal Additive Manufacturing: A Global Perspective," Metal Addit. Manuf., **2**(2), pp. 45–52.
[7] Weinong, W., and Chen, B. S., 2011, *Split Hopkinson (Kolsky) Bar*, Springer, New York.
[8] Ramesh, K. T., 2008, "High Rates and Impact Experiments," *Springer Handbook of Experimental Solid Mechanics*, Springer, Boston, MA, pp. 929–960.
[9] Voyiadjis, G. Z., Palazotto, A. N., and Gao, X.-L., 2002, "Modeling of Metallic Materials at High Strain Rates With Continuum Damage Mechanics," ASME Appl. Mech. Rev., **55**(5), pp. 481–492.
[10] Nicholas, T., 1972, "On the Determination of the Mechanical Properties of Materials at High Shear-Strain Rates," J. Mech. Phys. Solids, **20**(2), pp. 57–64.
[11] Veiga, C., Davim, J. P., and Loureiro, A. J. R., 2012, "Properties and Applications of Titanium Alloys: A Brief Review," Rev. Adv. Mater. Sci., **32**(2), pp. 133–148.
[12] Wulf, G. L., 1979, "High Strain Rate Compression of Titanium and Some Titanium Alloys," Int. J. Mech. Sci., **21**(12), pp. 713–718.
[13] Jones, D. R., Fensin, S. J., Dippo, O., Beal, R. A., Livescu, V., Martinez, D. T., Trujillo, C. P., Florando, J. N., Kumar, M., and Gray, G. T., 2016, "Spall Fracture in Additive Manufactured Ti-6Al-4V," J. Appl. Phys., **120**(13), p. 135902.
[14] Matthes, M., O'Toole, B., Trabia, M., Roy, S., Jennings, R., Bodenchak, E., Boswell, M., Graves, T., Hixson, R., Daykin, E., Hawkins, C., Fussell, Z., Daykin, A., and Heika, M., 2017, "Comparison of Failure Mechanisms Due to Shock Propagation in Forged, Layered, and Additive Manufactured Titanium Alloy," *Dynamic Behavior of Materials*, Vol. 1, Springer, New York, pp. 131–138.
[15] Ackelid, U., and Svensson, M., 2009, "Additive Manufacturing of Fully Dense TI6AL4V Metal Parts by Electron Beam Melting," International Conference Powder Metallurgy—Part: Material PowderMetal (PowderMet), Las Vegas, NV, June 28–July 1, pp. 9101–9109.
[16] Gray, G. T., III, Livescu, V., Rigg, P. A., Trujillo, C. P., Cady, C. M., Chen, S. R., Carpenter, J. S., Lienert, T. J., and Fensin, S., 2015, "Structure/Property (Constitutive and Dynamic Strength/Damage) Characterization of Additively Manufactured 316 L SS," EPJ Web Conf., **94**, p. 02006.
[17] Lovinger, Z., Rosenberg, Z., and Rittel, D., 2015, "On What Controls the Spacing of Spontaneous Adiabatic Shear Bands in Collapsing Thick-Walled Cylinders," EPJ Web Conf., **94**, p. 04054.
[18] Biswas, N., Ding, J. L., Balla, V. K., Field, D. P., and Bandyopadhyay, A., 2012, "Deformation and Fracture Behavior of Laser Processed Dense and Porous Ti6Al4V Alloy Under Static and Dynamic Loading," Mater. Sci. Eng. A, **549**, pp. 213–221.
[19] Wauthle, R., Ahmadi, S. M., Amin Yavari, S., Mulier, M., Zadpoor, A. A., Weinans, H., Van Humbeeck, J., Kruth, J.-P., and Schrooten, J., 2015, "Revival of Pure Titanium for Dynamically Loaded Porous Implants Using Additive Manufacturing," Mater. Sci. Eng. C, **54**, pp. 94–100.
[20] Furumoto, T., Koizumi, A., Alkahari, M. R., Anayama, R., Hosokawa, A., Tanaka, R., and Ueda, T., 2015, "Permeability and Strength of a Porous Metal Structure Fabricated by Additive Manufacturing," J. Mater. Process. Technol., **219**, pp. 10–16.
[21] Ben Shabat, Y., and Fischer, A., 2014, "Design of Adaptive Porous Micro-Structures for Additive Manufacturing," Proc. CIRP, **21**, pp. 133–137.
[22] Gorny, B., Niendorf, T., Lackmann, J., Thoene, M., Troester, T., and Maier, H. J., 2011, "In Situ Characterization of the Deformation and Failure Behavior of Non-Stochastic Porous Structures Processed by Selective Laser Melting," Mater. Sci. Eng. A, **528**(27), pp. 7962–7967.
[23] Wang, D., Yang, Y., Liu, R., Xiao, D., and Sun, J., 2013, "Study on the Designing Rules and Processability of Porous Structure Based on Selective Laser Melting (SLM)," J. Mater. Process. Technol., **213**(10), pp. 1734–1742.
[24] Taniguchi, N., Fujibayashi, S., Takemoto, M., Sasaki, K., Otsuki, B., Nakamura, T., Matsushita, T., Kokubo, T., and Matsuda, S., 2016, "Effect of Pore Size on Bone Ingrowth Into Porous Titanium Implants Fabricated by Additive Manufacturing: An In Vivo Experiment," Mater. Sci. Eng. C, **59**, pp. 690–701.
[25] Gurson, A. L., 1977, "Continuum Theory of Ductile Rupture by Void Nucleation and Growth—I: Yield Criteria and Flow Rules for Porous Ductile Media," ASME J. Eng. Mater. Technol., **99**(1), pp. 2–15.
[26] Benzerga, A. A., and Leblond, J.-B., 2010, "Ductile Fracture by Void Growth to Coalescence," Adv. Appl. Mech., **44**, pp. 169–305.
[27] Dongfang, M., Danian, C., Shanxing, W., Huanran, W., Canyuan, C., and Gaotao, D., 2011, "A Dynamic Investigation of Observable Void Growth and Coalescence in Pure Copper Sheets," J. Appl. Phys., **110**(9), p. 094905.
[28] Driemeier, L., Moura, R. T., Machado, I. F., and Alves, M., 2015, "A Bifailure Specimen for Accessing Failure Criteria Performance," Int. J. Plast., **71**, pp. 62–86.
[29] Weck, A., and Wilkinson, D. S., 2008, "Experimental Investigation of Void Coalescence in Metallic Sheets Containing Laser Drilled Holes," Acta Mater., **56**(8), pp. 1774–1784.
[30] Griffin, J. S., Butcher, C. J., and Chen, Z., 2014, "A Numerical and Experimental Investigation of Coalescence Between Cylindrical Holes," Trans. Can. Soc. Mech. Eng., **38**(1), pp. 93–106.
[31] da Silva, M. G., and Ramesh, K. T., 1997, "The Rate-Dependent Deformation and Localization of Fully Dense and Porous Ti-6Al-4V," Mater. Sci. Eng. A, **232**(1–2), pp. 11–22.
[32] Zhang, J., Wang, B., Lu, G., and Zhang, T. G., 2000, "Dynamic Yield Stresses of Porous Materials Made of Bronze and Iron," Key Eng. Mater., **177–180**(Pt.1), pp. 249–254.
[33] Lankford, J., Jr., and Dannemann, K. A., 1998, "Strain Rate Effects in Porous Materials," MRS Online Proc. Libr., **521**, pp. 103–108.
[34] Xue, P., Iqbal, N., Liao, H. J. J., Wang, B., and Li, Y. L. L., 2012, "Experimental Study, on Strain Rate Sensitivity of Ductile Porous Irons," Int. J. Impact Eng., **48**, pp. 82–86.
[35] Kolsky, H., 1949, "An Investigation of the Mechanical Properties of Materials at Very High Rates of Loading," Proc. Phys. Soc. B, **62**(11), p. 676.
[36] Harding, J., Wood, E. O., and Campbell, J. D., 1960, "Tensile Testing of Materials at Impact Rates of Strain," J. Mech. Eng. Sci., **2**(2), pp. 88–96.
[37] Rotbaum, Y., and Rittel, D., 2014, "Is There an Optimal Gauge Length for Dynamic Tensile Specimens?," Exp. Mech., **54**(7), pp. 1205–1214.
[38] EPMA, 2015, *Introduction to Additive Manufacturing Technology, a Guide for Designers and Engineers*, European Powder Metallurgy Association, Shrewsbury, UK, pp. 28–34.
[39] Kranz, J., Herzog, D., and Emmelmann, C., 2015, "Design Guidelines for Laser Additive Manufacturing of Lightweight Structures in TiAl6V4," J. Laser Appl., **27**(S1), p. S14001.
[40] Froes, F. H., and Staff, A. S. M. I., 2015, *Titanium: Physical Metallurgy Processing and Applications*, ASM International, Novelty, OH.
[41] Rittel, D., Rotbaum, Y., Rodríguez-Martínez, J. A., Sory, D., and Zaera, R., 2014, "Dynamic Necking of Notched Tensile Bars: An Experimental Study," Exp. Mech., **54**(6), pp. 1099–1109.
[42] Hibbitt, Karlsson and Sorensen, 1998, "ABAQUS/Standard User's Manual," Vol. 1, Hibbitt, Karlsson and Sorensen, Providence, RI.
[43] Qian, M., Xu, W., Brandt, M., and Tang, H. P., 2016, "Additive Manufacturing and Postprocessing of Ti-6Al-4V for Superior Mechanical Properties," MRS Bull., **41**(10), pp. 775–783.